geosciences

MDPI

Article

Rainfall-Induced Landslide Hazard Assessment Considering Multi-Temporal-Scale Rainfall Factors in Jiangwan Town, Shaoguan, Guangdong Province, China

Jing Yang [1], Dehe Yang [1,*], Zhima Zeren [1], Chong Xu [1,2], Yuandong Huang [1,2], Jianping Huang [1] and Hengxin Lu [1]

[1] National Institute of Natural Hazards, Ministry of Emergency Management of China, Beijing 100085, China
[2] Key Laboratory of Compound and Chained Natural Hazards Dynamics, Ministry of Emergency Management of China, Beijing 100085, China
* Correspondence: ydhmmm@163.com

Abstract

Shallow landslides triggered by extreme rainfall often occur abruptly and show pronounced spatial clustering. Accurate representation of rainfall conditions is therefore important for event-based landslide hazard assessment. This study investigated shallow landslides triggered by the April 2024 extreme rainfall event in Jiangwan Town, Guangdong Province, China. An event-based landslide inventory, half-hourly GPM IMERG precipitation data, and multiple environmental factors were used for hazard modelling. Three rainfall descriptors were considered: event cumulative rainfall, 21-day cumulative rainfall, and maximum 1 h rainfall. Controlled incremental experiments using Random Forest (RF) were conducted to evaluate the additional predictive information provided by these rainfall descriptors. RF, XGBoost, and an Artificial Neural Network (ANN) were then compared in terms of predictive performance. Incorporating all three rainfall descriptors increased the RF test-set AUC from 0.907 to 0.945. Among the three predefined rainfall descriptors, 21-day cumulative rainfall produced the largest incremental improvement. XGBoost achieved the highest overall predictive performance, with a test-set AUC of 0.971, and was selected for final hazard mapping. The high- and very-high-hazard zones predicted by XGBoost covered 33.2% of the study area and contained 89.7% of the observed landslide samples. These zones were concentrated mainly in the central and northeastern parts of Jiangwan Town. SHAP analysis identified elevation as the most influential predictor, while all three rainfall descriptors ranked among the important predictors. Overall, the results indicate that rainfall information at multiple temporal scales provides complementary predictive information and can improve event-conditioned shallow-landslide hazard assessment.

Keywords: rainfall-induced landslides; event-based hazard assessment; multi-temporal rainfall; machine learning; XGBoost; SHAP

Check for updates

Academic Editors: Ping Li, Dengfei Zhang and Mario Parise

Received: 24 June 2026
Revised: 23 August 2026
Accepted: 24 August 2026
Published: 2 September 2026

Copyright: © 2026 by the authors. Licensee MDPI, Basel, Switzerland. This article is an open access article distributed under the terms and conditions of the Creative Commons Attribution (CC BY) license.

1. Introduction

A landslide is the movement of a mass of rock, earth, or debris down a slope [1]. Rainfall is an important external trigger of landslides, particularly in mountainous and hilly regions [2]. Landslide occurrence is controlled by both relatively static predisposing conditions and dynamic rainfall forcing. The former include topography, geology, land cover, and anthropogenic disturbance, whereas the latter can be characterized by rainfall

intensity, duration, and cumulative rainfall [2,3]. Shallow landslides are particularly sensitive to rapid changes in hillslope hydrological conditions. They may occur suddenly and exhibit pronounced spatial clustering when intense rainfall occurs after or during prolonged wetting. Such conditions are common in the low-mountain and hilly regions of South China, where abundant rainfall, deeply weathered materials, dissected terrain, and intensive human disturbance often coexist. Therefore, event-based landslide hazard assessment should account for both the predisposing environmental conditions and the temporally varying rainfall conditions associated with the triggering event.

Machine learning models have been widely applied to landslide assessment because they can capture complex nonlinear relationships between landslide occurrence and multiple conditioning factors [4]. Physically based models generally require spatially detailed hydrological and geotechnical parameters, which are often difficult to obtain consistently at the regional scale [5]. In contrast, machine-learning methods provide a flexible framework for integrating heterogeneous environmental information. However, model performance depends not only on the learning algorithm but also on the selection and representation of conditioning factors, the representativeness of training samples, and the consistency of the modelling procedure. Random Forest (RF), Extreme Gradient Boosting (XGBoost), and Artificial Neural Network (ANN) models represent different machine-learning paradigms and have been widely applied to landslide assessment [6,7]. Their relative performance may vary across study areas, datasets, and factor configurations. Therefore, these models should be compared under consistent samples, predictors, and data-partitioning conditions. In addition to sample-level predictive performance and statistical comparisons, spatial consistency assessment provides complementary evidence for evaluating the consistency between predicted high-hazard areas and the observed spatial distribution of landslides. [8]. SHapley Additive exPlanations (SHAP) can further be used to quantify the contributions of individual predictors to model predictions and thereby improve model interpretability [9].

The temporal representation of rainfall conditions remains a key issue in event-based landslide hazard assessment. Static factors such as topography, lithology, land cover, and proximity to roads and rivers characterize the underlying predisposition to slope failure but cannot fully represent the temporal evolution of rainfall forcing and slope wetness during an extreme event [10]. Brunetti et al. [11] developed rainfall thresholds based on rainfall intensity and duration, demonstrating the importance of both rainfall magnitude and persistence. From a hydrological perspective, Bogaard and Greco [12] emphasized that rainfall triggering should be considered together with slope hydrological conditions rather than rainfall characteristics alone. Leonarduzzi and Molnar [13] further showed that hourly and daily rainfall information and antecedent wetness can provide different predictive information at the regional scale. More recently, Ren et al. [14] integrated maximum rolling rainfall over 2, 4, 6, 8, 12, 18, and 24 h durations into a dynamic rainfall index for spatiotemporal landslide susceptibility modelling. These studies collectively indicate that rainfall conditions relevant to landslide occurrence may operate over different temporal scales rather than being adequately represented by a single rainfall descriptor. Accordingly, this study used event cumulative rainfall, 21-day cumulative rainfall, and maximum 1 h rainfall to represent event-scale precipitation accumulation, longer-duration cumulative wetting preceding and accompanying the event, and short-duration rainfall intensity, respectively. The 21-day period was predefined according to the temporal characteristics of the April 2024 rainfall process and the above hydrological rationale, rather than selected through multi-window optimization; it is therefore treated as an event-specific cumulative-rainfall descriptor rather than an optimal temporal window.

The integration of rainfall information into event-conditioned hazard assessment requires a landslide inventory that can be explicitly associated with the target triggering event.

Mondini et al. [15] showed that event-based inventories document landslide populations generated by a single natural trigger and provide an important basis for event-specific susceptibility and hazard analyses, while also highlighting uncertainties associated with inventory construction. Oliveira et al. [16] further demonstrated that landslide patterns and their relationships with predisposing conditions can vary among rainfall events with contrasting triggering characteristics, particularly with respect to lithology and soil conditions. Their results further indicated that landslide susceptibility models developed using an inventory from a single event may have limited transferability to other events. These findings support the use of an event-specific inventory [17] for examining the response to a defined rainfall process, while emphasizing that the resulting relationships should be interpreted within the context of that event. Beyond this event-specific limitation, the use of such inventories for model development also introduces uncertainty in sample construction. Event-based inventories identify observed landslide locations but do not explicitly define true non-landslide locations. Consequently, the selection and environmental representativeness of non-landslide samples may also influence model reliability.

In April 2024, extreme rainfall in Jiangwan Town, Shaoguan City, Guangdong Province, triggered numerous shallow landslides. A previous study established an event-specific landslide inventory using high-resolution Planet satellite imagery and Normalized Difference Vegetation Index (NDVI) differencing and characterized the spatial distribution and major conditioning factors of these landslides. Building on this inventory, the present study focuses on the additional predictive information provided by rainfall at different temporal scales in event-conditioned landslide hazard assessment. Three predefined rainfall descriptors—event cumulative rainfall, 21-day cumulative rainfall, and maximum 1 h rainfall—are considered to represent event-scale rainfall accumulation, longer-duration rainfall accumulation, and short-duration rainfall intensity, respectively.

Accordingly, this study integrates the event-specific landslide inventory with half-hourly GPM IMERG precipitation data, lithology, and other environmental variables to assess shallow-landslide hazard associated with the April 2024 rainfall event in Jiangwan Town. Controlled incremental experiments using RF are first conducted to quantify the additional predictive contribution of each rainfall descriptor relative to the baseline environmental factors. The environmental representativeness of the selected non-landslide samples is then assessed by comparison with the eligible non-landslide candidate pool. Subsequently, RF, XGBoost, and ANN are evaluated under identical sample, predictor, and data-partitioning conditions through sample-level predictive performance, statistical comparison, and spatial consistency assessment. Based on the overall evaluation, the best-performing model is selected for final hazard mapping, and SHAP analysis is employed to interpret the relative contributions of individual predictors to model predictions. Overall, this study aims to assess the complementary predictive value of rainfall information at different temporal scales and to characterize the spatial pattern of shallow-landslide hazard associated with the April 2024 rainfall event.

2. Study Area

Jiangwan Town is located in the southwestern part of Wujiang District, Shaoguan City, Guangdong Province, China, extending approximately from 113°10′ E to 113°21′ E and from 24°32′ N to 24°43′ N (Figure 1). It borders Qujiang District to the east and Ruyuan Yao Autonomous County to the west. The study area is located in the transitional zone between the southern margin of the Nanling Mountains and the hilly region of northern Guangdong, and is characterized by typical low-mountain and hilly terrain of the Shaoguan region.

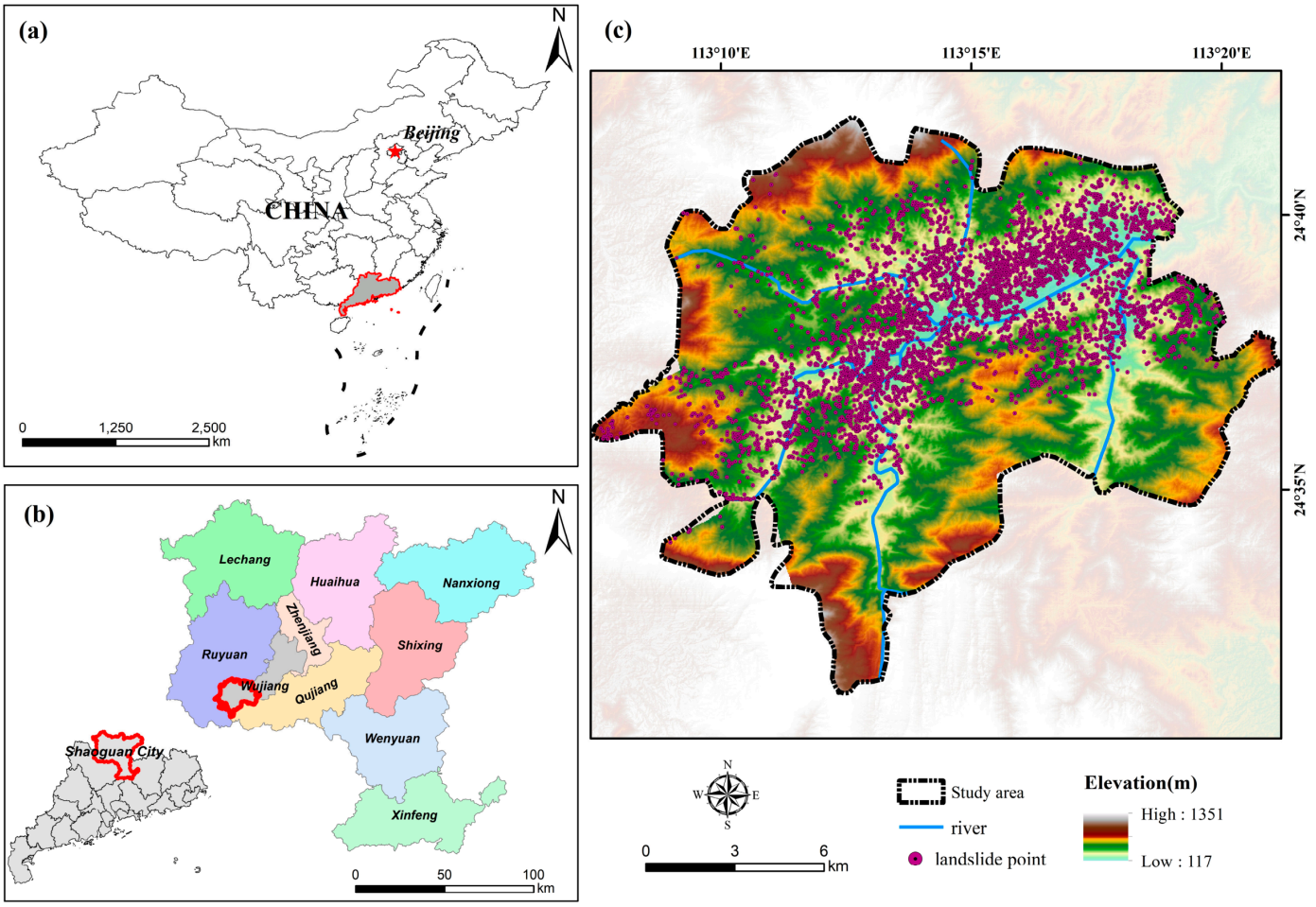

Figure 1. Geographic location, topographic background, and landslide inventory distribution of Jiangwan Town. (**a**) Location of Guangdong Province in China; (**b**) Location of Jiangwan Town in Shaoguan City; (**c**) Elevation, drainage network, and landslide distribution in Jiangwan Town. The red outlines in (**a**) and (**b**) indicate the highlighted locations of Guangdong Province and Jiangwan Town, respectively. (Map approval number: 0650).

The terrain is characterized by pronounced relief, with elevations ranging from approximately 117 to 1351 m. Well-developed mountain ridges, deeply incised valleys, and predominantly dendritic drainage networks form a characteristic ridge–slope–valley landscape. This geomorphological setting may promote surface-runoff concentration and slope-toe erosion, while lower slopes and valley margins commonly provide favourable locations for the accumulation of weathered and unconsolidated materials. Together, these conditions contribute to terrain settings that are susceptible to rainfall-induced shallow landslides [18]. The geological setting of Jiangwan Town is dominated by Early Jurassic granite, which underlies most of the study area. Late Jurassic granite occurs mainly as discontinuous bodies along the northern, western, and eastern margins. Devonian strata have a relatively limited distribution within the study area. The Yangxi Formation is exposed mainly near the northern boundary, whereas the Laohutou Formation occurs predominantly along the southern margin, with only minor local exposure in the north. Overall, the study area is characterized by a predominantly granitic geological background, whereas Devonian sedimentary units are confined mainly to peripheral zones. Variations in mineral composition, weathering resistance, and structural discontinuities among these lithological units may affect the formation, thickness, and mechanical properties of surficial weathered materials, thereby contributing to spatial differences in slope stability. The study area has a subtropical monsoon climate, with warm and humid conditions and marked

seasonal variability in precipitation [18]. Rainfall is concentrated mainly between April and August, when prolonged or high-intensity precipitation may induce marked changes in hillslope hydrological conditions.

Roads, settlements, and other engineering activities are concentrated mainly along river valleys, piedmont zones, and relatively gentle terrain. Local slope cutting, excavation, and alteration of natural drainage pathways may increase slope disturbance and enhance the local concentration of surface and subsurface water [19]. Together, these geological, geomorphological, climatic, and anthropogenic characteristics provide a regional mechanistic basis for incorporating lithology, topographic conditions, hydrological proximity, land cover, road-related disturbance, and rainfall conditions in the subsequent landslide hazard assessment.

3. Materials and Methods

3.1. Technical Workflow

The methodological framework comprised three main stages: data and sample preparation, model development and evaluation, and spatial interpretation (Figure 2). First, an event-specific landslide inventory, half-hourly GPM IMERG precipitation data, lithology, topographic variables, land cover, roads, and rivers were integrated to construct the candidate conditioning-factor system. Spatial preprocessing, rainfall-factor construction, positive- and negative-sample generation, and negative-sample representativeness assessment were then conducted. Second, factor redundancy was examined, after which RF rainfall-factor combination experiments and comparative modelling using RF, XGBoost, and ANN were performed under consistent sampling and data-partitioning conditions. All analyses were performed using Python (version 3.10). Machine-learning models and evaluation procedures were implemented using scikit-learn (version 1.3.2) and XGBoost (version 2.0.3), while SHAP interpretation was conducted using SHAP (version 0.44.1). Spatial data processing was conducted using ArcGIS 10.8 (Esri, Redlands, CA, USA). Finally, sample-level metrics, cross-validation, the DeLong test, spatial consistency assessment, frequency ratios, and SHAP analysis were jointly used to evaluate and interpret the modelling results.

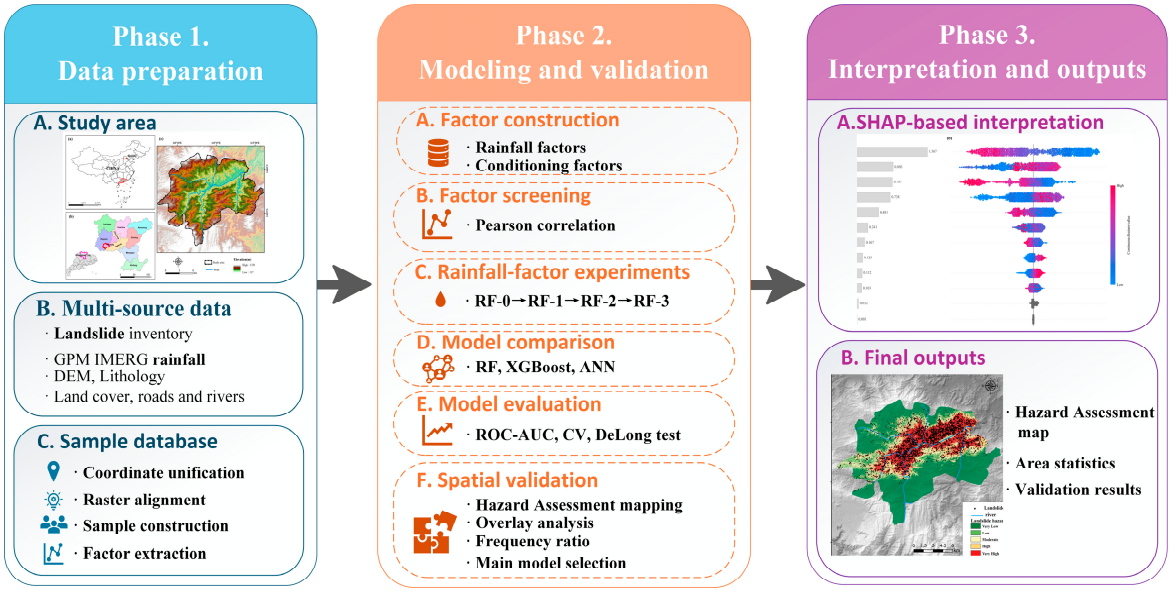

Figure 2. Technical Workflow Diagram.

3.2. Data Sources and Factor Construction

This study integrated an event-specific landslide inventory with GPM IMERG precipitation data, Copernicus DEM, land-cover data, lithological information, and road and river datasets. The spatial resolution, data source, and preprocessing procedure of each dataset are summarized in Table 1, while the resulting analytical factors are presented in Figure 3.

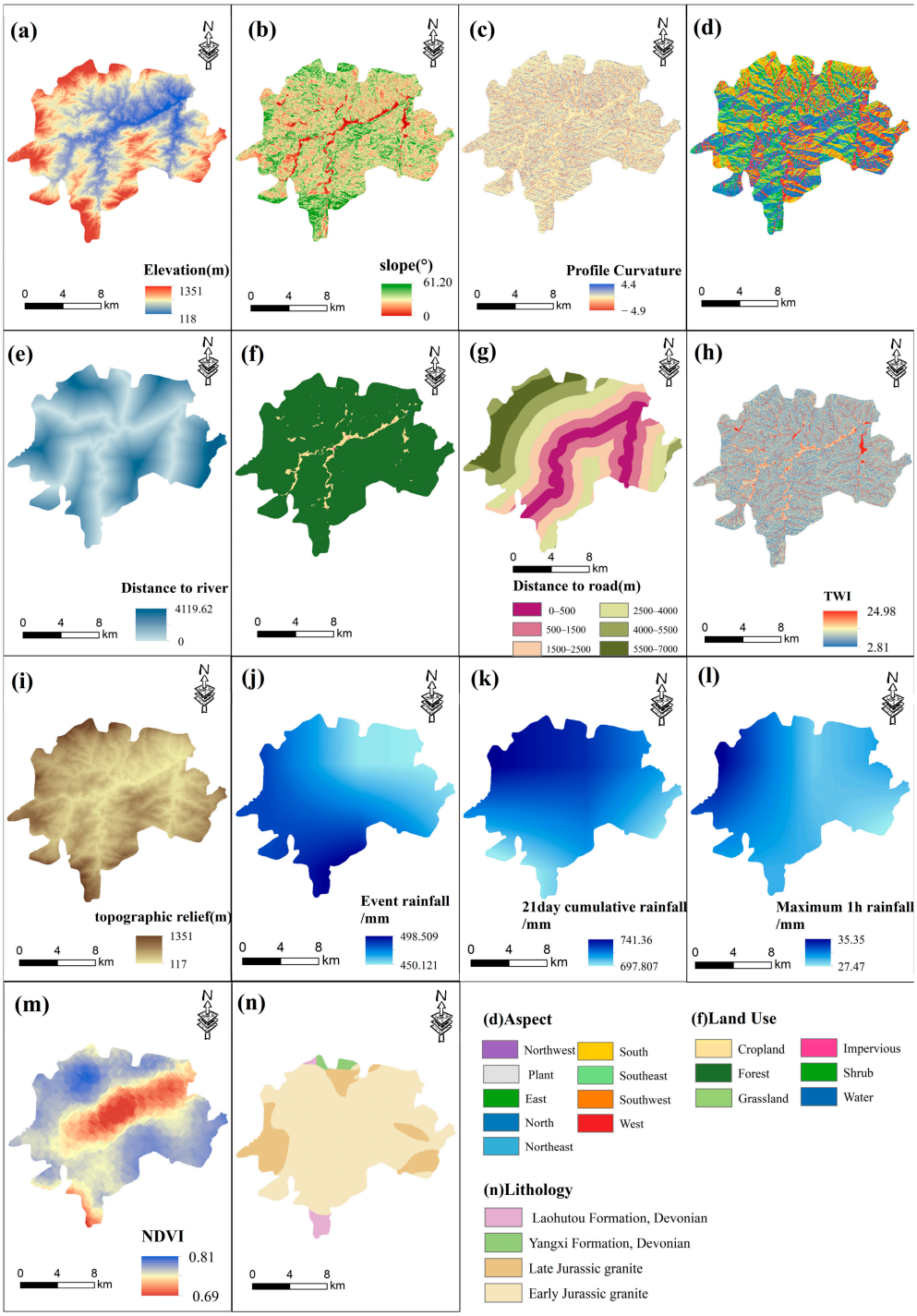

Figure 3. Landslide Hazard Assessment Factors. (**a**) Elevation; (**b**) Slope; (**c**) Profile curvature; (**d**) Aspect; (**e**) Distance to rivers; (**f**) Land use; (**g**) Distance to road; (**h**) Topographic Wetness Index (TWI); (**i**) Topographic relief; (**j**) Event cumulative rainfall; (**k**) 21-day cumulative rainfall; (**l**) Maximum 1-h rainfall; (**m**) Normalized Difference Vegetation Index (NDVI); (**n**) Lithology. The categorical legends for aspect, land use, and lithology are provided on the right side of the figure.

3.2.1. Event-Specific Landslide Inventory

The landslide inventory used in this study was derived from the event-based shallow-landslide dataset established by Huang et al. [20] for the April 2024 extreme rainfall event in Shaoguan, Guangdong Province. The original inventory was compiled through visual interpretation of high-resolution pre- and post-event remote-sensing imagery and field verification, and included 6310 shallow landslides across the affected area. For the present study, the inventory was clipped to the administrative boundary of Jiangwan Town and further subjected to spatial and data-quality screening. After linkage with the conditioning-factor database and removal of records with incomplete or invalid predictor information, 5402 landslide samples were retained as positive samples for subsequent model development.

Table 1. Data Sources and Evaluation Factors.

Data Type	Factor	Data Source	Resolution
Rainfall data	Rain event, Rain21d, Rain1hmax	GPM IMERG Final Run V07 [21]	0.1°
Topographical data	Elevation	Copernicus DEM GLO-30 [22]	30 m
	Slope	from DEM	
	Aspect	from DEM	
	Profile curvature	from DEM	
	Topographic Wetness Index (TWI)	from DEM	
	Topographic relief	from DEM	
Geological data	Lithology	Spatial Database of the National 1:200,000 Digital Geological Map of China [19]	1:200,000
Land cover	Land cover classification	China Land Cover Dataset (CLCD) [23]	30 m
Hydrological data	Distance to river	National Geomatics Center of China (https://www.ngcc.cn)	1:1,000,000
Road data	Distance to roads	National Geomatics Center of China (https://www.ngcc.cn)	1:1,000,000

3.2.2. Rainfall Data and Rainfall-Factor Construction

Half-hourly precipitation data were obtained from the GPM IMERG Final Run V07 product, with a native spatial resolution of 0.1° × 0.1° and a temporal resolution of 30 min [22]. Precipitation is provided as a rainfall rate (mm h^{-1}); therefore, the rainfall amount for each 30 min interval was calculated by multiplying the corresponding rate by 0.5 h. All timestamps were converted from Coordinated Universal Time (UTC) to Beijing Time (UTC + 8) prior to temporal aggregation. Based on the temporal evolution of the GPM precipitation series and previous analyses of the April 2024 rainfall event, the period from 16 to 21 April 2024 was defined as the main event-rainfall window.

Based on the temporally standardized precipitation series, three rainfall descriptors were constructed to characterize complementary temporal aspects of the rainfall process (Figure 4). Event cumulative rainfall (Rain_event) was calculated by summing the half-hourly rainfall amounts over the main event window and was used to represent event-scale precipitation accumulation. The 21-day cumulative rainfall (Rain21d), calculated for the period from 1 to 21 April, was used to characterize longer-duration cumulative rainfall conditions before and during the event. Because this period partially overlaps the

main event window, Rain21d should not be interpreted as a strictly antecedent-rainfall variable. Maximum 1 h rainfall (Rain1hmax) was defined as the maximum moving sum of two consecutive half-hourly rainfall amounts within the main event window and was used to represent short-duration rainfall intensity. The 21-day accumulation period was predefined on the basis of the temporal characteristics of the target rainfall process and the hydrometeorological rationale outlined in Section 1, rather than selected through systematic optimization of multiple accumulation windows. Accordingly, Rain21d is treated as an event-specific longer-duration rainfall descriptor rather than as an empirically optimized temporal window.

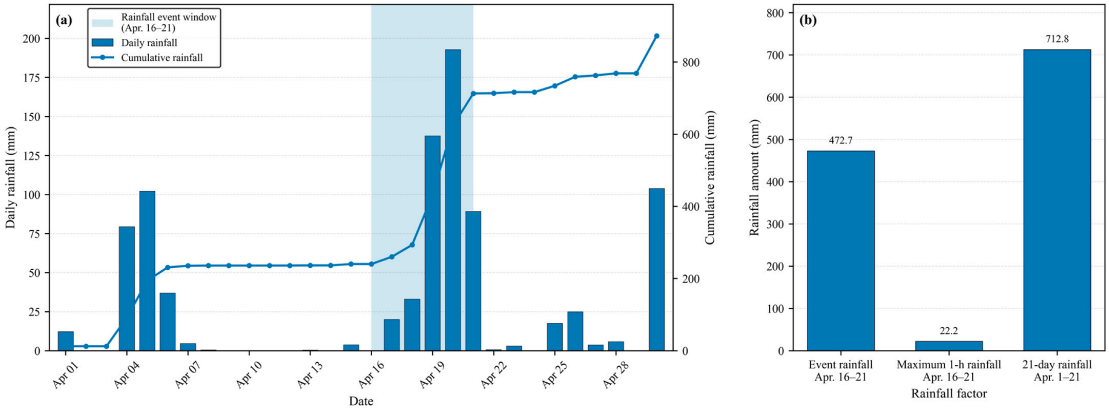

Figure 4. Rainfall process and statistics of rainfall factors in Jiangwan Town in April 2024. (**a**) Temporal variation of daily rainfall and cumulative rainfall, with the shaded area indicating the main rainfall event window (16–21 April 2024); (**b**) Comparison of rainfall amounts represented by the three rainfall descriptors, including event cumulative rainfall, maximum 1-h rainfall, and 21-day cumulative rainfall.

For subsequent integration with the environmental predictors, the three derived rainfall-factor rasters were reprojected and resampled onto the common 30 m modelling grid using bilinear interpolation. This step was performed solely to ensure spatial consistency among the model inputs and did not increase the intrinsic spatial resolution of the precipitation data. Thus, although the rainfall variables were represented on a 30 m grid for model input, their effective spatial information remained constrained by the native 0.1° resolution of the GPM IMERG product.

3.3. Spatial Preprocessing and Factor Representation

All spatial datasets, including the study-area boundary, landslide inventory, and conditioning factors, were transformed to a common projected coordinate system and clipped to the administrative boundary of Jiangwan Town. Raster-based conditioning factors were subsequently aligned to a common 30 m modelling grid with consistent spatial extent, cell size, and pixel registration. Continuous raster variables were resampled using interpolation methods appropriate for continuous data, whereas categorical variables, including land use and lithology, were resampled using the nearest-neighbour method to preserve their original class values. The GPM-derived rainfall factors were aligned to the same modelling grid using bilinear interpolation, following the procedure described in Section 3.2.2.

Following spatial harmonization, continuous conditioning factors were retained as numerical variables in their original physical units, whereas land use and lithology were treated as categorical variables. Missing, invalid, and anomalous raster values were identified during preprocessing to prevent invalid cells from entering the subsequent sample-construction procedure. The resulting spatially aligned factor layers constituted the common predictor database used for sample extraction and subsequent modelling.

3.4. Sample Construction and Representativeness Assessment

Mapped landslides were used as positive samples. To define the non-landslide candidate pool, mapped landslide polygons and their surrounding 150 m buffer zones were excluded. Water bodies, built-up areas, and cells containing invalid predictor values were also removed. The 150 m buffer zone was adopted as a conservative exclusion distance to minimize the chance of selecting pseudo-absence samples in proximity to mapped landslides. Zones immediately adjacent to known landslides may include disturbed slopes, transitional areas, or landslide bodies that have not been fully mapped. This buffer served solely as a criterion for sampling exclusion.

Non-landslide samples were randomly drawn from the eligible candidate cells. To maintain class balance, 5402 non-landslide samples were selected to match the 5402 positive landslide samples. The final sample database therefore contained 10,804 samples. Binary labels were assigned, with landslide samples coded as 1 and non-landslide samples coded as 0.

The environmental representativeness of the selected non-landslide samples was evaluated by comparison with the full eligible non-landslide candidate pool. For continuous predictors, empirical cumulative distribution functions (ECDFs) were compared, and distributional similarity was quantified using the overlap coefficient (OVL) [24]. For categorical predictors, including land use and lithology, category proportions were compared and total variation distance (TVD) [25] was used to quantify distributional differences. Aspect was treated separately because of its circular nature [26] and was evaluated descriptively rather than as an ordinary linear variable. In addition, a direction-independent single-factor AUC was calculated for each predictor to characterize the environmental separability between landslide and non-landslide samples [27]. This analysis was used to describe class separability and was not used as a measure of negative-sample representativeness.

The final sample database was divided into training, validation, and test sets using stratified random sampling. These subsets accounted for 52.5%, 17.5%, and 30.0% of the total samples, respectively. The same data partition and random seed were used for all rainfall-factor experiments and model comparisons. This ensured that differences in model performance were evaluated under consistent sampling and data-partitioning conditions.

3.5. Correlation Analysis and Factor Screening

To identify potential redundancy among predictors, Pearson correlation analysis was performed on the 14 candidate conditioning factors before training the RF, XGBoost, and ANN models. Pearson correlation coefficients were calculated for all pairs of factors to quantify their linear relationships. An absolute correlation coefficient of 0.70 was used as a reference threshold for identifying strong pairwise correlations [28]. When strong correlations were detected, factor removal was determined by considering both statistical redundancy and the physical relevance of the variables to rainfall-induced shallow landslides. The Pearson correlation coefficient was calculated as follows [29]:

$$r = \frac{\sum_{i=1}^{n}\left(X_i - \overline{X}\right)\left(Y_i - \overline{Y}\right)}{\sqrt{\sum_{i=1}^{n}\left(X_i - \overline{X}\right)^2}\sqrt{\sum_{i=1}^{n}\left(Y_i - \overline{Y}\right)^2}} \quad (1)$$

where X_i and Y_i denote the (i)-th sample values of the two evaluation factors, respectively; X_i and Y_i represent the mean values of the corresponding factors.

3.6. Stepwise Rainfall-Factor Combination Experiments

To assess whether the predefined rainfall indicators provided additional predictive information beyond the baseline environmental factors, four progressively nested RF models were constructed. The incremental effect was defined as the change in model

performance after adding one rainfall indicator to the preceding model, while keeping the sample partition, environmental predictors, RF configuration, and evaluation procedure unchanged. Because the rainfall indicators were introduced in a predefined sequence, the resulting performance changes are conditional on the order of addition. They should therefore be interpreted as incremental predictive gains rather than as independent or causal effects of individual rainfall variables.

Following this incremental design, RF-0 was used as the baseline model with nine environmental predictors. Rain_event, Rain21d, and Rain1hmax were then sequentially introduced in RF-1, RF-2, and RF-3, respectively. The predictor combinations and corresponding experimental objectives are summarized in Table 2.

Table 2. RF Settings for the Stepwise Rainfall-Factor Combination Experiments.

Model	Input Factor Combination	Objective
RF-0	Elevation, Slope, Aspect, Profile Curvature, TWI, Land Use, Lithology, Distance to Road, Distance to River	Establish the baseline model using environmental factors only
RF-1	RF-0 + Rain event	Assess the performance change associated with adding event cumulative rainfall.
RF-2	RF-1 + Rain21d	Assess whether the broader 1–21 April cumulative rainfall provides additional information beyond Rain_event.
RF-3	RF-2 + Rain1hmax	Assess whether maximum 1 h rainfall provides further supplementary information.

3.7. Model Evaluation and Spatial Consistency Assessment

Model performance was evaluated at both the sample and spatial levels. At the sample level, Accuracy, Precision, Recall, F1-score, Cohen's kappa coefficient, and the area under the receiver operating characteristic curve (AUC) were calculated. AUC was used as the primary measure of overall discriminatory performance. Pairwise differences in test-set AUC were assessed using the DeLong test [30] for both the rainfall-factor experiments and the comparison among RF, XGBoost, and ANN. A p-value of <0.05 was considered statistically significant.

For spatial consistency assessment, the trained models were applied to all valid 30 m analysis cells to generate continuous event-conditioned landslide probabilities. A common five-class Jenks natural-breaks scheme was used to allow enable comparison among the RF, XGBoost, and ANN hazard maps [31]. The full-grid prediction probabilities from the three models were pooled, and four common breakpoints were derived from the pooled distribution. The resulting thresholds were 0.1289, 0.3323, 0.5853, and 0.8312. These thresholds defined five hazard classes: very low ($\leq$0.1289), low (0.1289–0.3323), moderate (0.3323–0.5853), high (0.5853–0.8312), and very high (>0.8312). The same thresholds were applied to all three models to avoid differences caused solely by model-specific classification schemes.

The mapped landslides were then overlaid on the classified hazard maps. For each hazard class, the proportion of the total valid analysis area and the proportion of mapped landslides were calculated. Landslide concentration was quantified using the Frequency Ratio [32,33]:

$$FR_i = \frac{L_i / L}{A_i / A} \quad (2)$$

where L_i is the number of mapped landslides in class i, L is the total number of mapped landslides, A_i is the area of class, and A is the total valid analysis area. An FR_i value greater than 1 indicates relative landslide enrichment within the corresponding class. Stronger spatial concentration was indicated when the high and very high hazard classes occupied a relatively small proportion of the study area but contained a large proportion of

mapped landslides and exhibited high FR values. Because the landslide inventory used in this assessment also contributed to model development, these results were interpreted as evidence of spatial consistency and concentration rather than as independent spatial consistency assessment.

Based on the combined sample-level and spatial evaluation, a final model was selected for hazard mapping and interpretation. SHAP analysis was then applied to this model to examine the contributions of individual predictors [34,35]. Mean absolute SHAP values were used to quantify global feature importance. Signed SHAP values were used to examine the direction and magnitude of predictor contributions to model output. Because SHAP explains model predictions rather than causal relationships, the results were interpreted in conjunction with the geological, geomorphological, hydrological, rainfall, and anthropogenic characteristics of the study area.

4. Results

4.1. Factor Screening and Pairwise Correlation Analysis

Fourteen candidate factors were initially considered for the correlation analysis. The analysis identified a perfect positive correlation between terrain relief and elevation (r = 1.00), indicating substantial redundancy between the two variables. Terrain relief was therefore excluded, while elevation was retained because of its clearer physical interpretation in regional landslide assessment. NDVI was also removed according to the predefined factor-screening criterion. Apart from the correlation between terrain relief and elevation, all pairwise absolute Pearson correlation coefficients were below 0.70. After screening, 12 factors were retained, with no strong pairwise linear correlations observed among the final predictors. The correlation structure and factor-screening results are shown in Figure 5.

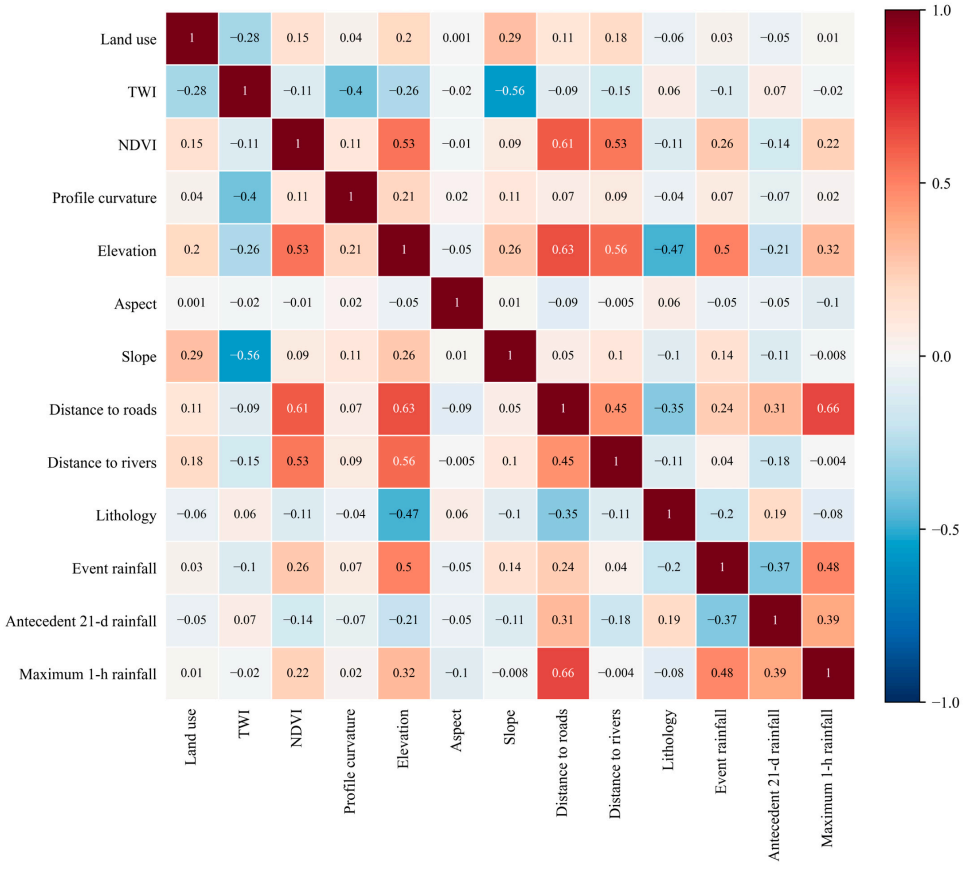

Figure 5. Pearson Correlation Matrix of Evaluation Factors.

4.2. Environmental Representativeness of Non-Landslide Samples

After spatial exclusion and data-quality screening, 161,291 cells remained in the eligible non-landslide candidate pool. From this pool, 5402 non-landslide samples were randomly selected to match the number of landslide samples. The representativeness assessment showed that the selected negatives preserved the main environmental characteristics of the full candidate population (Figure 6).

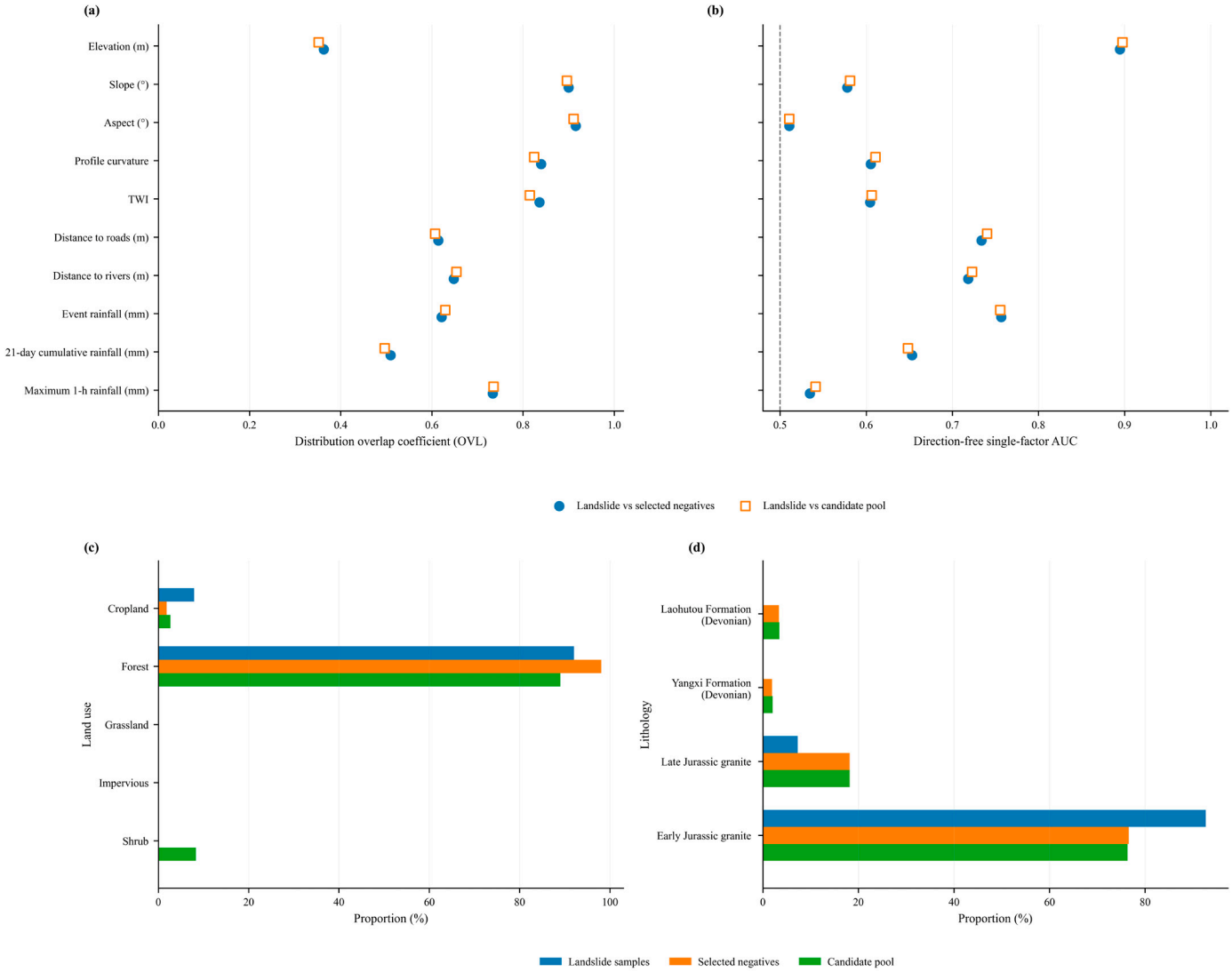

Figure 6. Representativeness of the selected negative samples. (**a**) Distribution overlap coefficients and (**b**) direction-free single-factor AUC values obtained using the selected negative samples and the complete candidate pool as alternative non-landslide references; the dashed line in panel (**b**) indicates the reference level of AUC = 0.5, representing random discrimination; proportions of (**c**) land-use and (**d**) lithological categories among the landslide samples, selected negatives, and complete candidate pool.

For the continuous predictors, the results obtained using the selected negatives were highly consistent with those based on the full candidate pool. Differences in both distributional overlap and single-factor separability were small, indicating that random sampling did not substantially alter the environmental relationship between landslide and non-landslide conditions. Elevation showed the strongest separation between the two classes, but this pattern remained nearly unchanged when the full candidate pool was used. This suggests that the pronounced elevation-related separation mainly reflects the spatial distribution of the mapped landslides rather than a substantial bias introduced by negative sampling.

The categorical predictors showed a similar pattern. Lithological composition was highly consistent between the selected negatives and the full candidate pool, whereas land use showed a modest difference in class proportions. However, this difference did not increase the separation between the landslide and non-landslide samples. Overall, no substantial environmental bias was identified in the selected negative samples, supporting their use in the subsequent rainfall-factor experiments and model comparisons.

4.3. Incremental Predictive Value of Rainfall Factors

The sequential inclusion of the three rainfall factors progressively improved RF performance (Figure 7). Compared with the baseline model, the full rainfall-factor configuration increased the test-set AUC from 0.907 to 0.945. Pairwise DeLong tests showed that the AUC improvement at each incremental step was statistically significant (Table 3). These results indicate that rainfall information provided additional predictive value beyond the baseline environmental factors.

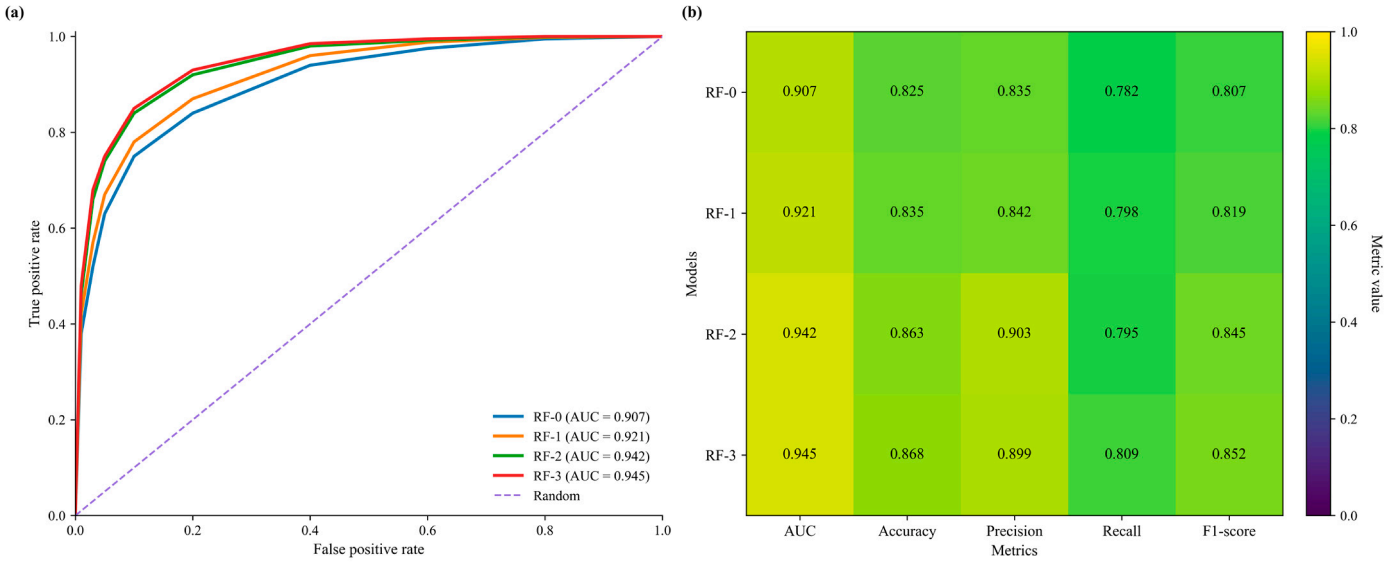

Figure 7. Predictive performance of RF models with sequential inclusion of rainfall factors: (**a**) test-set ROC curves; (**b**) comparison of AUC, Accuracy, Precision, Recall, and F1-score.

Table 3. Pairwise DeLong test results for RF models with different rainfall-factor combinations.

Comparison	AUC_1	AUC_2	ΔAUC *	Z-Value	*p*-Value	Significance
RF-0 vs. RF-1	0.9073	0.9208	0.0135	9.2105	<0.001	significant
RF-1 vs. RF-2	0.9208	0.9416	0.0208	10.480	<0.001	significant
RF-2 vs. RF-3	0.9416	0.9450	0.0034	6.990	<0.001	significant
RF-0 vs. RF-3	0.9073	0.9450	0.0377	13.4455	<0.001	significant

* Note: ΔAUC denotes the increase in AUC of the latter model relative to the preceding model; ($p < 0.05$) indicates that the difference is statistically significant. The significance of the DeLong test depends not only on the magnitude of ΔAUC but also on the standard error of the AUC difference. Therefore, the results should be interpreted comprehensively in conjunction with the actual performance increment and other evaluation metrics.

The magnitude of the improvement differed among the three incremental steps. The largest gain occurred when 21-day cumulative rainfall was added after event cumulative rainfall. Event cumulative rainfall produced a smaller but clear improvement over the baseline model, whereas the subsequent addition of maximum 1 h rainfall resulted in only a limited further increase in performance. Under the predefined sequence of factor addition, the results therefore suggest that longer-duration cumulative rainfall provided

the strongest incremental predictive information, while short-duration rainfall intensity mainly supplied supplementary information.

The relatively strong improvement associated with Rain21d supports its usefulness as a longer-duration rainfall descriptor for this event. However, the result does not imply that a 21-day accumulation period is universally optimal.

4.4. Comparison of Model Predictive Performance

RF, XGBoost, and ANN were evaluated using the same 12-factor system and identical data partitions. All three models showed strong discrimination and classification performance on the independent test set (Figure 8). XGBoost achieved the best overall performance, followed closely by ANN, whereas RF showed comparatively lower performance.

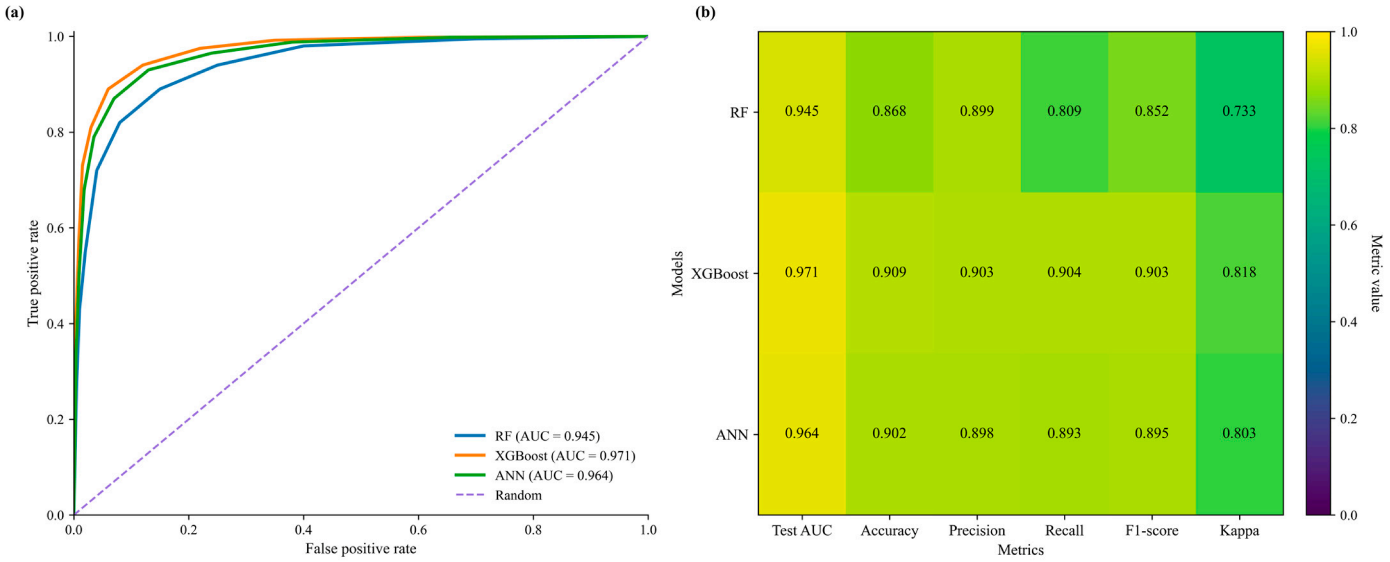

Figure 8. Predictive performance of the three machine-learning models: (**a**) test-set ROC curves; (**b**) comparison of test-set classification metrics.

The DeLong test confirmed significant differences in test-set AUC among all three models (Table 4). Both XGBoost and ANN significantly outperformed RF. XGBoost also achieved a significantly higher AUC than ANN, although the absolute difference between the two models was small. This indicates that the statistical difference between XGBoost and ANN corresponded to only a modest difference in sample-level discriminatory performance.

Table 4. Pairwise DeLong test results for RF, XGBoost, and ANN.

Comparison	AUC_1	AUC_2	ΔAUC	Z-Value	*p*-Value	Significance
RF vs. XGBoost	0.945	0.971	0.0261	11.648	<0.001	significant
RF vs. ANN	0.945	0.964	0.0190	7.702	<0.001	significant
XGBoost vs. ANN	0.971	0.964	−0.0071	−5.046	<0.001	significant

Overall, XGBoost provided the strongest sample-level predictive performance, with ANN yielding closely comparable results. RF remained effective but was consistently less competitive in the overall evaluation. Because sample-level metrics alone do not capture the spatial characteristics of hazard predictions, the three models were further compared in terms of spatial hazard distribution and landslide concentration.

4.5. Spatial Consistency of Hazard Zoning

The three models produced broadly consistent hazard patterns, with high and very high hazard zones generally corresponding to areas of dense mapped landslide occurrence (Figure 9). However, the spatial extent of these zones differed among the models. XGBoost and ANN delineated broader high-hazard areas and captured larger proportions of the mapped landslides, whereas RF produced a more spatially restricted pattern.

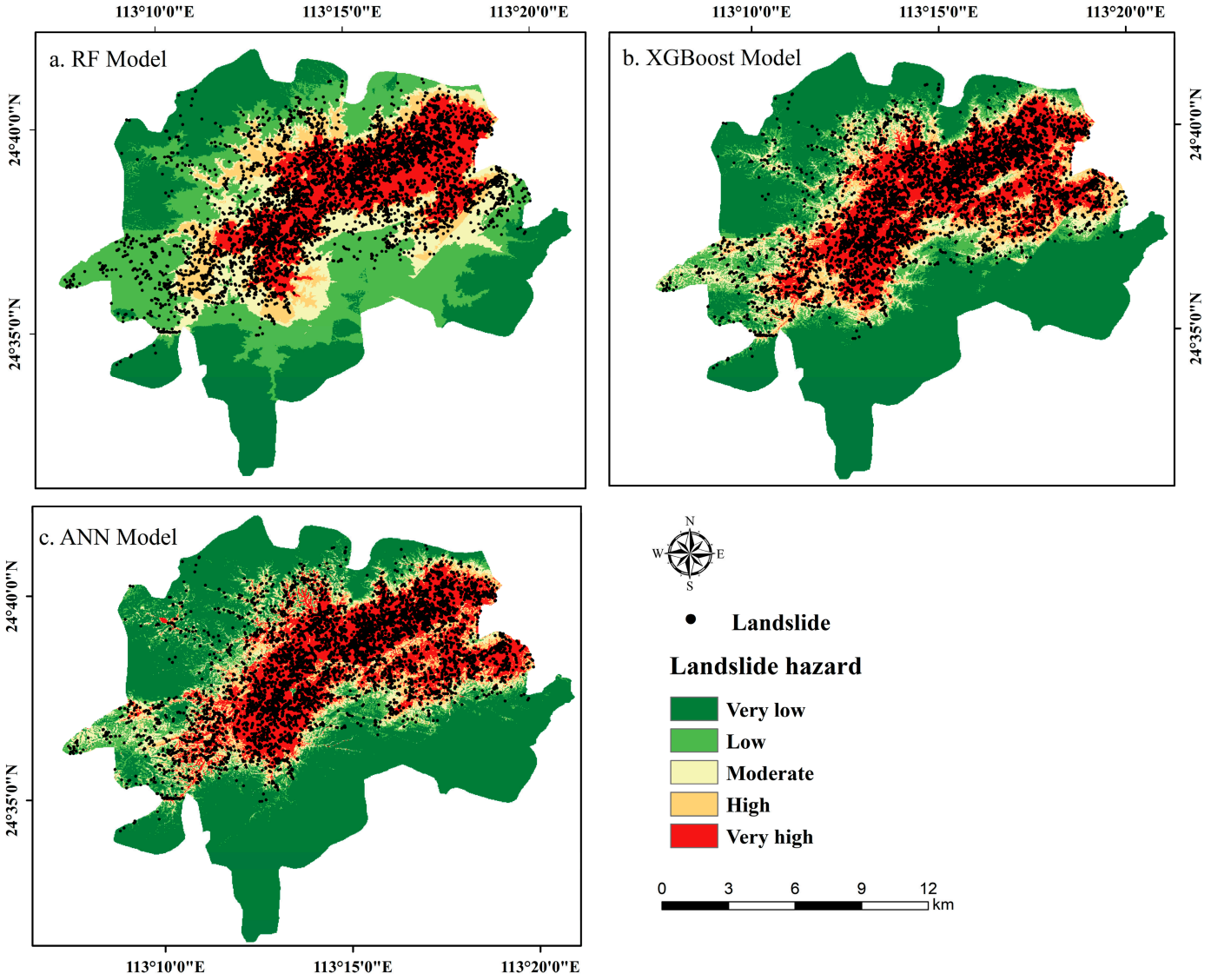

Figure 9. Spatial distribution of landslide hazard predicted by (**a**) RF, (**b**) XGBoost, and (**c**) ANN, with the mapped landslides overlaid for spatial consistency assessment.

The spatial statistics revealed a clear trade-off between landslide coverage and spatial concentration (Table 5). XGBoost achieved the highest landslide coverage within the combined high and very high hazard zones, with ANN showing a similar pattern. RF covered a smaller area but yielded slightly higher FR values, indicating a more concentrated delineation of mapped landslides. Across the hazard classes, landslide concentration increased toward the higher hazard levels, supporting the internal spatial consistency of the three classifications.

Table 5. Spatial consistency assessment Results for the Very-High and Combined High–Very-High Hazard Zones of Different Models.

Model	Very High Area/%	Very High Landslide/%	FR	High + Very High Area/%	High + Very High Landslide/%	FR
RF	18.776	63.276	3.370	28.406	78.117	2.750
XGBoost	23.250	77.525	3.334	33.216	89.698	2.700
ANN	24.345	77.432	3.181	33.008	88.568	2.683

When considered together with the sample-level results in Section 4.4, XGBoost provided the best overall balance between predictive performance and spatial landslide coverage. RF showed slightly stronger spatial concentration but lower sample-level performance and lower landslide coverage. XGBoost was therefore selected for the final hazard mapping and subsequent model interpretation. RF was retained as the reference model for the incremental rainfall-factor experiments. Because the same landslide inventory contributed to model development, these spatial results are interpreted as evidence of spatial consistency and concentration rather than as independent validation.

4.6. Spatial Pattern of the XGBoost-Based Hazard Map

Based on the combined sample-level and spatial evaluation, XGBoost was selected as the final model for hazard mapping. The resulting spatial distribution is shown in Figure 10.

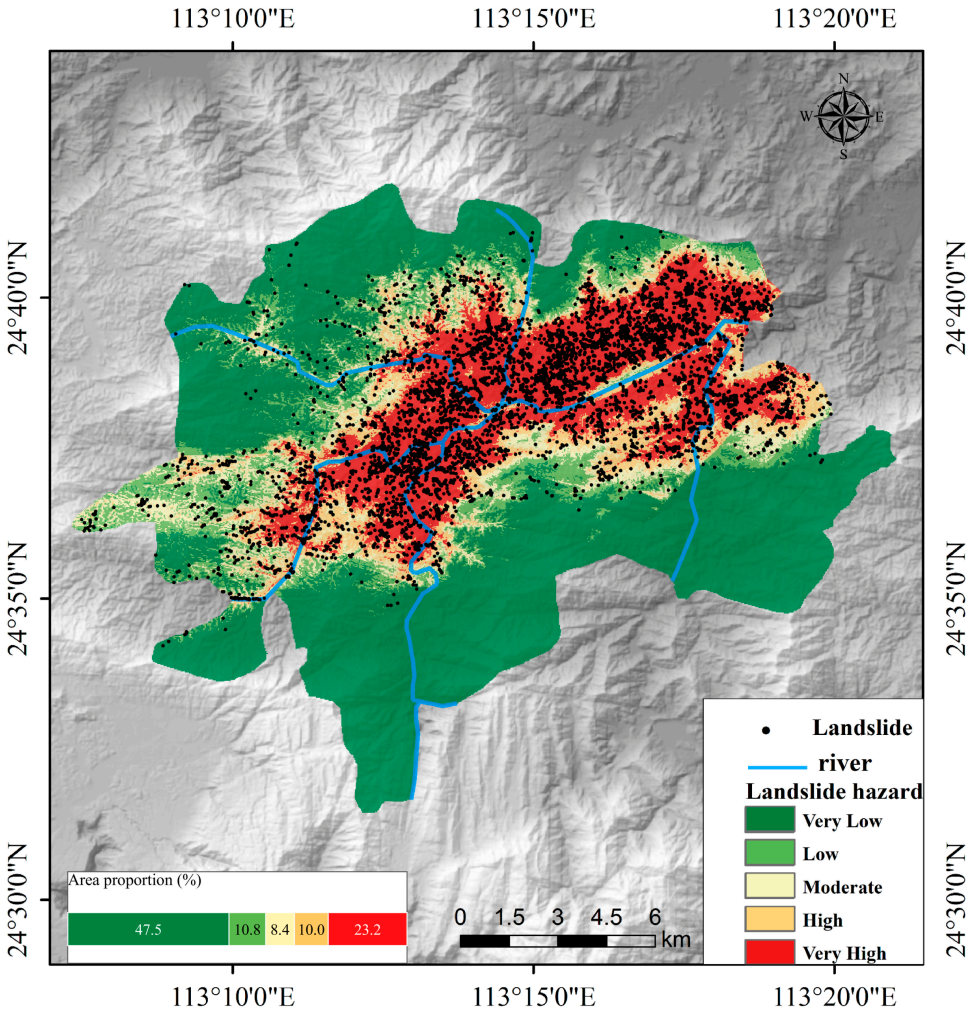

Figure 10. XGBoost-based landslide hazard zoning in Jiangwan Town. The inset shows the area proportions of the five hazard classes.

The predicted hazard shows clear spatial heterogeneity across Jiangwan Town. High and very high hazard zones are concentrated mainly in the central and northeastern parts of the study area, where they form a relatively continuous belt. Smaller high-hazard patches also occur in the western and eastern sectors. These areas generally coincide with the main concentrations of mapped landslides. In contrast, low and very low hazard zones are more widely distributed in the peripheral and southern parts of the study area, where mapped landslides are relatively sparse. Moderate hazard zones mainly occur between the high-hazard belt and the surrounding lower-hazard areas.

The combined high and very high hazard zones occupy approximately one-third of the study area. The detailed area proportions of the five hazard classes are shown in Figure 10. Overall, the XGBoost-based hazard map identifies a spatially concentrated high-hazard corridor that is broadly consistent with the observed distribution of event landslides. The predictor contributions associated with this spatial pattern are further examined using SHAP analysis in the following section.

4.7. SHAP-Based Interpretation of XGBoost Predictions

SHAP analysis was used to interpret the predictor contributions in the final XGBoost model (Figure 11). Global importance was evaluated using mean absolute SHAP values. Signed SHAP values were used to examine whether individual predictor values tended to increase or decrease the model output. Land use and lithology were treated as categorical predictors and were therefore not interpreted according to a continuous low-to-high value scale.

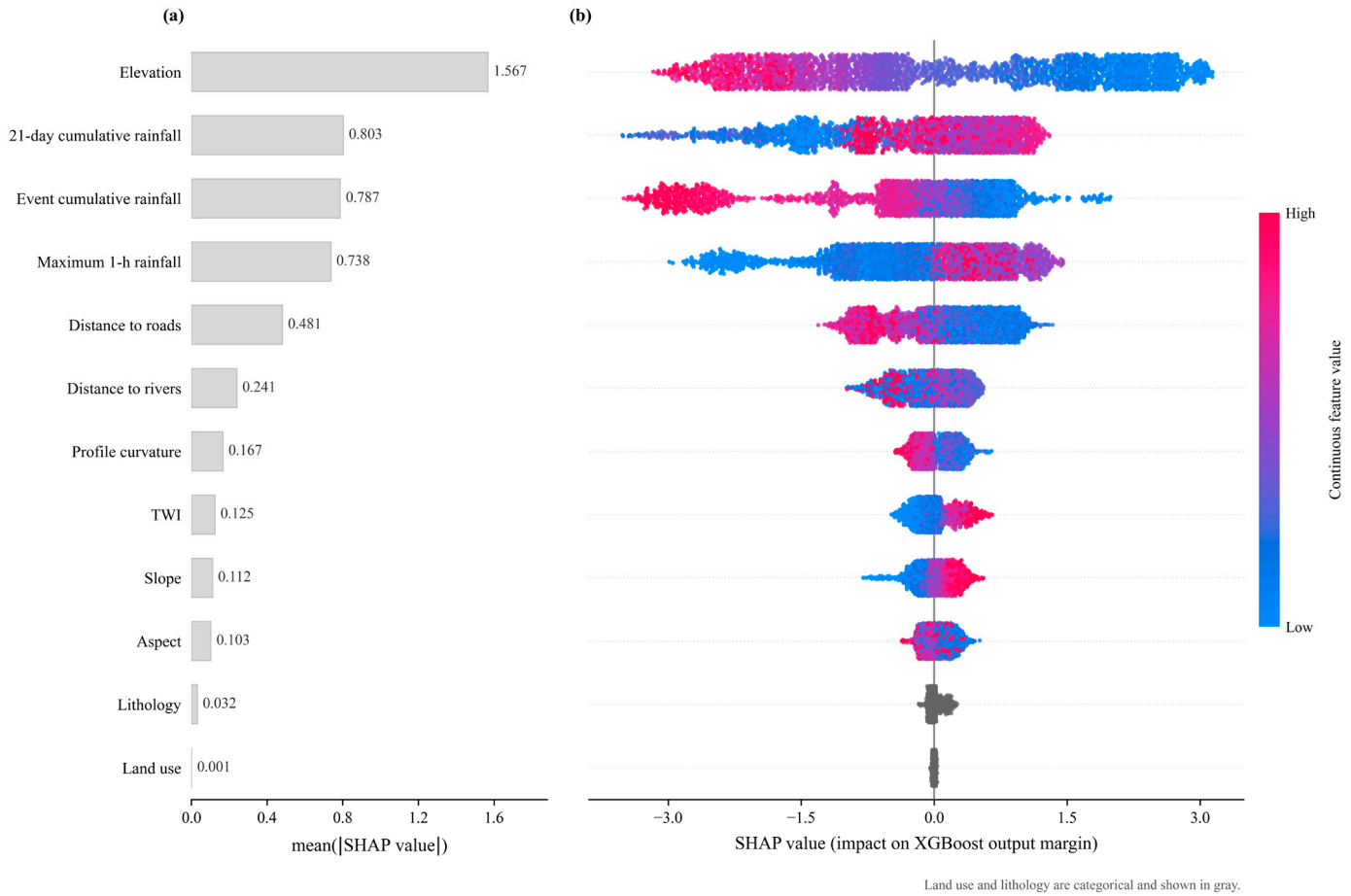

Figure 11. SHAP-based interpretation of the final XGBoost model: (**a**) global feature importance quantified by mean absolute SHAP values; (**b**) SHAP-value distributions of the 12 retained predictors.

Elevation was the most influential predictor in the final model. The three rainfall variables also ranked among the leading predictors. Among them, 21-day cumulative rainfall had the highest global importance, followed by event cumulative rainfall and maximum 1 h rainfall. This ranking is consistent with the incremental experiment in Section 4.3, where the addition of 21-day cumulative rainfall produced the largest performance gain among the three rainfall steps. Taken together, these results indicate that rainfall information at different temporal scales contributed substantially to the XGBoost predictions.

The SHAP distributions also showed different directional patterns among the leading predictors. Lower elevations were generally associated with positive SHAP values, whereas higher elevations tended to reduce the model output. Higher 21-day cumulative rainfall and maximum 1 h rainfall were more frequently associated with positive SHAP values. Event cumulative rainfall showed a different pattern, with higher values occurring mainly on the negative side of the SHAP distribution. Shorter distances to roads were also more commonly associated with positive model contributions. These patterns reflect conditional associations within the fitted XGBoost model and may depend on the joint effects of multiple predictors. They should therefore not be interpreted as direct causal relationships with landslide occurrence.

5. Discussion

5.1. Hydrological Implications of Multi-Temporal Rainfall Information

Rainfall-induced shallow landslides are influenced by rainfall conditions operating over different temporal scales rather than by a single rainfall descriptor [12,13]. Previous studies have shown that rainfall intensity, duration, and cumulative amount can all contribute useful information for landslide assessment, although their relative importance varies among regions and events [11,13]. Bogaard and Greco [12] emphasized the interaction between longer-term hydrological conditions and short-term meteorological forcing, while Leonarduzzi and Molnar [13] showed that rainfall information at different temporal resolutions can provide complementary information on landslide occurrence. The present results are consistent with this general framework. In the incremental RF experiments, the addition of 21-day cumulative rainfall produced the largest predictive gain among the three rainfall steps. In the final XGBoost model, all three rainfall descriptors also showed relatively high SHAP importance. Together, these results suggest that rainfall conditions associated with the April 2024 event were better represented by information from multiple temporal scales than by a single rainfall indicator.

The three rainfall descriptors capture different aspects of the rainfall process. Rain21d includes rainfall both before and during the main event and therefore represents a longer-duration rainfall accumulation background rather than strictly antecedent rainfall. Such prolonged rainfall may progressively alter soil-water and infiltration conditions and thereby modify slope sensitivity to subsequent rainfall [36,37]. Rain_event represents precipitation accumulation during the main event window, whereas Rain1hmax characterizes short-duration rainfall intensity. Their combined predictive relevance suggests that longer-duration accumulation, event-scale rainfall, and short-duration intensity provide partly complementary information. This interpretation is consistent with previous studies showing that shallow landslides may be associated with both intense short-duration rainfall and prolonged rainfall sequences [13].

The SHAP results also show that the contribution of rainfall variables depends on the broader predictor context. In particular, event cumulative rainfall did not exhibit a simple pattern in which higher values consistently increased model output. This indicates that its predictive contribution was conditional on the combination of rainfall and environmental factors represented in the model. Topography, lithology, drainage conditions,

and anthropogenic disturbance may modify how similar rainfall conditions are associated with slope instability [4,12]. Rainfall should therefore be interpreted together with spatial conditioning factors rather than as an isolated predictor [4]. Overall, the results support the use of multi-temporal rainfall information in event-conditioned landslide assessment. However, the relatively strong contribution of Rain21d applies only to the April 2024 event and to the predefined rainfall descriptors examined here. It should not be interpreted as evidence that a 21-day accumulation window is universally optimal.

5.2. Environmental and Geological Interpretation of the Spatial Hazard Pattern

The spatial pattern of predicted hazard reflects the combined influence of terrain, rainfall, drainage conditions, and human disturbance. Elevation showed the highest global importance in the XGBoost model, but its role should not be interpreted as a direct causal effect. In this study, lower elevations were generally associated with higher model outputs. This pattern may partly reflect the concentration of landslides along valley-side slopes and other dissected terrain within the event-affected area. Elevation may also capture spatial variation related to drainage position and the distribution of human activities [21]. This interpretation is consistent with previous observations of the April 2024 event, which reported marked landslide clustering along river corridors and valley-side slopes in Jiangwan Town [18,20].

Road proximity also contributed substantially to the model predictions. Shorter distances to roads were generally associated with positive SHAP contributions. Road construction can alter slope geometry, disturb natural drainage, and expose weathered slope materials [38]. These processes may increase local sensitivity to rainfall-induced instability. However, the observed SHAP pattern represents a spatial association within the fitted model. It does not demonstrate that road construction directly caused the mapped landslides.

The inclusion of lithology allowed regional geological heterogeneity to be represented explicitly in the hazard model. Its SHAP importance was lower than that of the dominant topographic and rainfall predictors. Nevertheless, lithology remains physically relevant because different rock units can produce weathering profiles and surficial materials with different properties. Previous studies in northern Guangdong have reported that strongly weathered granitic materials and granite-derived residual soils can provide susceptible material conditions for rainfall-induced shallow failures [39,40]. Lithological classes, however, do not directly describe slope-scale properties such as weathering depth, soil thickness, hydraulic conductivity, cohesion, or internal friction angle [41]. Lithology should therefore be interpreted as a regional indicator of geological background rather than as a direct measure of slope stability.

Overall, the spatial hazard pattern is best interpreted as the modelled outcome of interacting rainfall, terrain, geological, hydrological, and anthropogenic conditions. The high-hazard corridor identified by XGBoost should therefore not be attributed to any single predictor. Instead, it reflects the combined environmental conditions represented in the model under the April 2024 rainfall event.

5.3. Robustness and Methodological Uncertainty

The construction of non-landslide samples remains an important source of uncertainty in data-driven landslide hazard assessment. Different sampling strategies may alter the environmental characteristics of the training data and thereby affect model predictions [42,43]. In this study, the selected negative samples retained the main environmental characteristics of the eligible candidate pool. This result suggests that random sampling did not introduce substantial environmental bias into the final sample set. The 150 m buffer was used as a conservative exclusion distance to reduce the likelihood of selecting

pseudo-absence samples close to mapped landslides. Such areas may include disturbed slopes, uncertain landslide boundaries, or unmapped failures. However, buffer distance and negative-sampling strategy can influence susceptibility modelling results [44,45]. The adopted 150 m distance should therefore be regarded as a sampling criterion rather than an optimal threshold. Its suitability may also depend on inventory completeness and the spatial density of event landslides.

The comparison among RF, XGBoost, and ANN also shows that model performance depends on the evaluation criterion considered. XGBoost performed best at the sample level and provided high landslide coverage in the upper hazard classes. RF produced a more spatially concentrated high-hazard pattern. These differences reflect a trade-off between classification performance, spatial coverage, and landslide concentration rather than a contradiction between the evaluation results. Previous studies have similarly shown that the relative performance of machine-learning models can vary with sampling strategy, predictor configuration, and study-area characteristics [42,46]. No single algorithm should therefore be assumed to be universally superior. In this study, XGBoost was selected for final hazard mapping based on the combined sample-level and spatial assessment. RF was retained as the reference model for the incremental rainfall-factor experiments.

Hazard classification introduces a further source of uncertainty. Different classification methods and threshold schemes can alter the mapped extent of individual hazard classes and the apparent concentration of landslides within them [47,48]. A common Jenks classification scheme was adopted here to ensure direct comparison among the RF, XGBoost, and ANN maps. However, sensitivity to alternative classification thresholds was not systematically examined. The reported area proportions and FR values should therefore be interpreted as conditional on the adopted classification scheme. Sample-level predictive metrics provided the primary quantitative basis for model comparison, while class-based spatial coverage and landslide concentration were used as complementary evidence. This distinction helps avoid attributing differences caused by map classification directly to differences in model predictive ability.

5.4. Contributions, Limitations, and Future Directions

The main contribution of this study is the integration of an event-specific landslide inventory with rainfall information at multiple temporal scales within a consistent modelling framework. The framework combines incremental rainfall-factor experiments, model comparison, spatial consistency assessment, and SHAP-based interpretation. Lithology was also incorporated into the predictor system, and the environmental representativeness of the selected non-landslide samples was explicitly evaluated. Together, these components provide an integrated approach for assessing rainfall-related predictive information in event-conditioned landslide hazard modelling. Several limitations should be considered when interpreting the results, as follows.

First, the analysis was based on a single extreme rainfall event in Jiangwan Town. The identified rainfall–landslide relationships and model performance are therefore event-dependent and may not be directly transferable to other events [16]. Future studies should include multiple rainfall–landslide events to evaluate the stability and transferability of the modelling framework and rainfall-factor contributions.

Second, the 21-day cumulative rainfall period was predefined rather than selected through systematic comparison of alternative accumulation windows. Its relatively strong contribution in this study therefore does not indicate that 21 days represents an optimal rainfall window [13]. Future work should evaluate multiple accumulation periods to determine how sensitive model performance and rainfall contributions are to the selected temporal window.

Third, the native spatial resolution of the GPM IMERG V07 precipitation product is approximately 0.1°. Resampling to the 30 m modelling grid was performed only for spatial alignment and did not increase the intrinsic spatial information of the precipitation data. This limitation may restrict the representation of local rainfall variability in mountainous terrain [49]. Future studies could integrate rain-gauge, weather-radar, and satellite precipitation observations to improve the spatial characterization of rainfall [49,50].

Fourth, although the environmental representativeness of the selected non-landslide samples was explicitly evaluated and common Jenks thresholds were consistently applied to RF, XGBoost, and ANN, two sources of methodological uncertainty remain. The adopted 150 m landslide-exclusion buffer was not selected through a systematic sensitivity analysis, and different exclusion distances may alter the composition of the non-landslide candidate population and consequently affect model performance. Similarly, the spatial statistics derived from classified hazard maps remain conditional on the adopted hazard-classification scheme, because sensitivity to alternative classification methods or thresholds was not systematically examined. Therefore, the 150 m buffer should be regarded as a conservative sampling criterion rather than an optimal threshold, while the reported class-area proportions and FR values should be interpreted as complementary spatial evidence rather than classification-independent measures of predictive performance. Future studies should systematically evaluate multiple buffer distances, negative-sampling strategies, and hazard-classification schemes to quantify these sources of uncertainty and assess the robustness of the resulting spatial comparisons.

Finally, lithology provides only a regional representation of geological conditions. It does not directly describe slope-scale properties such as weathering depth, residual-soil thickness, hydraulic conductivity, cohesion, internal friction angle, or groundwater conditions [41]. Field investigation, geotechnical testing, and hydrological monitoring would therefore be valuable for improving the process-based interpretation of model predictions.

Given these limitations, the resulting hazard map should be interpreted as a relative spatial assessment conditioned on the April 2024 extreme rainfall event. It should not be interpreted as a long-term probability of landslide occurrence [51].

6. Conclusions

This study developed an event-conditioned shallow-landslide hazard assessment for the April 2024 extreme rainfall event in Jiangwan Town. An event-based landslide inventory was integrated with multi-temporal rainfall information, environmental factors, lithology, and machine-learning models. The main conclusions are as follows.

(1) Multi-temporal rainfall information improved model performance beyond the baseline environmental factors. In the RF incremental experiments, the test-set AUC increased from 0.907 to 0.945 after the three rainfall descriptors were sequentially introduced. The largest incremental gain occurred after the addition of 21-day cumulative rainfall, followed by event cumulative rainfall, while maximum 1 h rainfall provided a smaller supplementary gain. These results indicate that the three rainfall descriptors provided different and complementary predictive information for this event.

(2) XGBoost achieved the best overall sample-level performance among the three models, with a test-set AUC of 0.971. It also provided high landslide coverage within the high and very high hazard zones. RF produced a slightly more spatially concentrated high-hazard pattern but showed lower overall predictive performance. XGBoost was therefore selected for final hazard mapping, while RF was retained for the rainfall-factor incremental experiments.

(3) The XGBoost hazard map showed clear spatial heterogeneity, with high and very high hazard zones concentrated mainly from central Jiangwan Town toward the northeast. SHAP analysis showed that elevation made the largest contribution to model predictions,

while all three rainfall descriptors also showed substantial contributions. Among the rainfall variables, 21-day cumulative rainfall had the highest global SHAP importance. These contributions represent associations within the fitted model and should be interpreted together with the geological, geomorphological, hydrological, and anthropogenic context of the study area.

Overall, the results support the use of multi-temporal rainfall information in event-conditioned shallow-landslide hazard assessment. The resulting hazard map represents relative spatial hazard associated with the April 2024 event rather than a long-term probability of landslide occurrence.

Author Contributions: J.Y. and D.Y.; methodology, J.Y. and D.Y.; validation, D.Y. and Y.H.; formal analysis, J.Y., J.H. and H.L.; resources, D.Y., Z.Z. and C.X.; data curation, J.Y. and Y.H.; writing—original draft preparation, J.Y.; writing—review and editing, J.Y., D.Y., Z.Z. and C.X.; visualization, J.Y.; funding acquisition, Z.Z., C.X., J.H. and H.L. All authors have read and agreed to the published version of the manuscript.

Funding: This research was funded by the National Key R&D Program of Intergovernmental Cooperation in Science and Technology (Grant No. 2023YFE0117300) and the National Key Research and Development Program of China (Grant No. 2024YFC3012604).

Data Availability Statement: The GPM IMERG precipitation data and Copernicus DEM data used in this study are available from their respective public data repositories. The land-cover, road, river, and landslide inventory data were obtained from the sources described in the Data and Methods sections. The processed datasets generated and analyzed during the current study are available from the corresponding author upon reasonable request. Some third-party data are subject to the terms and restrictions of their original data providers and therefore cannot be publicly redistributed.

Acknowledgments: The authors acknowledge the NASA Global Precipitation Measurement mission and the NASA Goddard Earth Sciences Data and Information Services Center for providing the GPM IMERG Final Run V07 precipitation data. The authors also acknowledge the European Union and the European Space Agency for providing the Copernicus DEM GLO-30 data, the CLCD research team for providing the China Land Cover Dataset, and the National Geomatics Center of China for providing the road and river data. The authors gratefully acknowledge the Key Laboratory of Compound and Chained Natural Hazards Dynamics, Ministry of Emergency Management of China, for providing the landslide inventory data. During the preparation of this manuscript, the authors used the Nano Banana Pro model for the purpose of generating several illustrative figures. The authors have reviewed and edited the output and take full responsibility for the accuracy and integrity of the figures and the overall content of this publication.

Conflicts of Interest: The authors declare no conflicts of interest.

References

1. Aleotti, P.; Chowdhury, R. Landslide hazard assessment: Summary review and new perspectives. *Bull. Eng. Geol. Environ.* **1999**, *58*, 21–44. [CrossRef]
2. Wu, C.-H.; Chen, S.-C. Determining landslide susceptibility in Central Taiwan from rainfall and six site factors using the analytical hierarchy process method. *Geomorphology* **2009**, *112*, 190–204. [CrossRef]
3. Chen, C.-W.; Saito, H.; Oguchi, T. Rainfall intensity–duration conditions for mass movements in Taiwan. *Prog. Earth Planet. Sci.* **2015**, *2*, 14. [CrossRef]
4. Van Westen, C.J.; Castellanos, E.; Kuriakose, S.L. Spatial data for landslide susceptibility, hazard, and vulnerability assessment: An overview. *Eng. Geol.* **2008**, *102*, 112–131. [CrossRef]
5. Alvioli, M.; Baum, R.L. Parallelization of the TRIGRS model for rainfall-induced landslides using the message passing interface. *Environ. Model. Softw.* **2016**, *81*, 122–135. [CrossRef]
6. Zhang, W.; Ali, M.Z.; Cui, W.; Sun, C.; Zheng, Z.; Chen, K. Severe rainfall-induced landslides in Pingyuan County, Guangdong, China, in June 2024: W. Zhang et al. *Landslides* **2025**, *22*, 2623–2639.

7. Zhang, A.; Zhao, X.-W.; Zhao, X.-Y.; Zheng, X.-Z.; Zeng, M.; Huang, X.; Wu, P.; Jiang, T.; Wang, S.-C.; He, J.; et al. Comparative study of different machine learning models in landslide susceptibility assessment: A case study of Conghua District, Guangzhou, China. *China Geol.* **2024**, *7*, 104–115. [CrossRef]
8. Yang, L.; Cui, Y.; Xu, C.; Ma, S. Application of coupling physics–based model TRIGRS with random forest in rainfall-induced landslide-susceptibility assessment: Yang, Cui, Xu and Ma. *Landslides* **2024**, *21*, 2179–2193.
9. Al-Najjar, H.; Kalantar, B.; Pradhan, B.; Beydoun, G.; Ueda, N. Remote Sensing; Sciences, S.I. Shapley additive explanations (SHAP) for landslide susceptibility models: Shedding light on explainable AI. *ISPRS Ann. Photogramm. Remote Sens. Spat. Inf. Sci.* **2025**, *X-G-2025*, 81–85.
10. Catani, F.; Lagomarsino, D.; Segoni, S.; Tofani, V. Landslide susceptibility estimation by random forests technique: Sensitivity and scaling issues. *Nat. Hazards Earth Syst. Sci.* **2013**, *13*, 2815–2831. [CrossRef]
11. Brunetti, M.T.; Peruccacci, S.; Rossi, M.; Luciani, S.; Valigi, D.; Guzzetti, F. Rainfall thresholds for the possible occurrence of landslides in Italy. *Nat. Hazards Earth Syst. Sci.* **2010**, *10*, 447–458. [CrossRef]
12. Bogaard, T.; Greco, R. Invited perspectives: Hydrological perspectives on precipitation intensity-duration thresholds for landslide initiation: Proposing hydro-meteorological thresholds. *Nat. Hazards Earth Syst. Sci.* **2018**, *18*, 31–39. [CrossRef]
13. Leonarduzzi, E.; Molnar, P. Deriving rainfall thresholds for landsliding at the regional scale: Daily and hourly resolutions, normalisation, and antecedent rainfall. *Nat. Hazards Earth Syst. Sci.* **2020**, *20*, 2905–2919. [CrossRef]
14. Ren, T.; Gao, L.; Gong, W. An ensemble of dynamic rainfall index and machine learning method for spatiotemporal landslide susceptibility modeling. *Landslides* **2024**, *21*, 257–273. [CrossRef]
15. Mondini, A.C.; Viero, A.; Cavalli, M.; Marchi, L.; Herrera, G.; Guzzetti, F. Comparison of event landslide inventories: The Pogliaschina catchment test case, Italy. *Nat. Hazards Earth Syst. Sci.* **2014**, *14*, 1749–1759. [CrossRef]
16. Oliveira, S.C.; Zêzere, J.L.; Garcia, R.A.; Pereira, S.; Vaz, T.; Melo, R. Landslide susceptibility assessment using different rainfall event-based landslide inventories: Advantages and limitations. *Nat. Hazards* **2024**, *120*, 9361–9399. [CrossRef]
17. Huang, F.; Mao, D.; Jiang, S.-H.; Zhou, C.; Fan, X.; Zeng, Z.; Catani, F.; Yu, C.; Chang, Z.; Huang, J.; et al. Uncertainties in landslide susceptibility prediction modeling: A review on the incompleteness of landslide inventory and its influence rules. *Geosci. Front.* **2024**, *15*, 101886. [CrossRef]
18. Wei, R.; Shan, Y.; Wang, L.; Peng, D.; Qu, G.; Qin, J.; He, G.; Fan, L.; Li, W. Clustered rainfall-induced landslides in Jiangwan Town, Guangdong, China during April 2024: Characteristics and controlling factors. *Remote Sens.* **2025**, *17*, 2635. [CrossRef]
19. Li, C.; Wang, X.; He, C.; Wu, X.; Kong, Z.; Li, X. National 1: 200000 digital geological map (public version) spatial database. *Geol. China* **2019**, *46*, 1–10.
20. Huang, Y.; Xu, C.; Liu, Y.; He, X.; Shao, X.; Zhao, B.; Kong, X. Inventory and distribution feature of shallow landslides triggered by heavy rain event in Shaoguan, Guangdong Province in April 2024. *Chin. J. Geol. Hazard Control* **2025**, *36*, 28–42.
21. Huffman, G.J.; Bolvin, D.T.; Braithwaite, D. GPM IMERG Final Run Version 07. NASA Goddard Earth Sciences Data and Information Services Center (GES DISC), 2023. Available online: https://disc.gsfc.nasa.gov/ (accessed on 23 August 2026).
22. Simard, M.; Denbina, M.; Marshak, C.; Neumann, M.J. A global evaluation of radar-derived digital elevation models: SRTM, NASADEM, and GLO-30. *J. Geophys. Res. Biogeosci.* **2024**, *129*, e2023JG007672. [CrossRef]
23. Yang, J.; Huang, X. The 30 m annual land cover dataset and its dynamics in China from 1990 to 2019. *Earth Syst. Sci. Data* **2021**, *13*, 3907–3925. [CrossRef]
24. Inman, H.F.; Bradley, E.L., Jr. The overlapping coefficient as a measure of agreement between probability distributions and point estimation of the overlap of two normal densities. *Commun. Stat.-Theory Methods* **1989**, *18*, 3851–3874. [CrossRef]
25. Gibbs, A.L.; Su, F.E. On choosing and bounding probability metrics. *Int. Stat. Rev.* **2002**, *70*, 419–435. [CrossRef]
26. Jammalamadaka, S.R.; Sengupta, A. *Topics in Circular Statistics*; World Scientific: Singapore, 2001; Volume 5.
27. Hanley, J.A.; McNeil, B.J. The meaning and use of the area under a receiver operating characteristic (ROC) curve. *Radiology* **1982**, *143*, 29–36. [CrossRef]
28. Dormann, C.F.; Elith, J.; Bacher, S.; Buchmann, C.; Carl, G.; Carré, G.; Marquéz, J.R.G.; Gruber, B.; Lafourcade, B.; Leitão, P.J.; et al. Collinearity: A review of methods to deal with it and a simulation study evaluating their performance. *Ecography* **2013**, *36*, 27–46. [CrossRef]
29. Pearson, K. Note on regression and inheritance in the case of two parents. *Proc. R. Soc. Lond.* **1895**, *58*, 240–242. [CrossRef]
30. DeLong, E.R.; DeLong, D.M.; Clarke-Pearson, D.L. Comparing the areas under two or more correlated receiver operating characteristic curves: A nonparametric approach. *Biometrics* **1988**, *44*, 837–845. [CrossRef] [PubMed]
31. Jenks, G.F.; Caspall, F.C. Error on choroplethic maps: Definition, measurement, reduction. *Ann. Assoc. Am. Geogr.* **1971**, *61*, 217–244. [CrossRef]
32. Lee, S.; Talib, J.A. Probabilistic landslide susceptibility and factor effect analysis. *Environ. Geol.* **2005**, *47*, 982–990. [CrossRef]
33. Lee, S.; Pradhan, B. Landslide hazard mapping at Selangor, Malaysia using frequency ratio and logistic regression models. *Landslides* **2007**, *4*, 33–41. [CrossRef]
34. Lundberg, S.M.; Lee, S.-I. A unified approach to interpreting model predictions. *Adv. Neural Inf. Process. Syst.* **2017**, *30*, 4765–4774.

35. Lundberg, S.M.; Erion, G.; Chen, H.; DeGrave, A.; Prutkin, J.M.; Nair, B.; Katz, R.; Himmelfarb, J.; Bansal, N.; Lee, S.-I. From local explanations to global understanding with explainable AI for trees. *Nat. Mach. Intell.* **2020**, *2*, 56–67. [CrossRef] [PubMed]
36. Iverson, R.M. Landslide triggering by rain infiltration. *Water Resour. Res.* **2000**, *36*, 1897–1910. [CrossRef]
37. Leonarduzzi, E.; McArdell, B.W.; Molnar, P. Rainfall-induced shallow landslides and soil wetness: Comparison of physically based and probabilistic predictions. *Hydrol. Earth Syst. Sci.* **2021**, *25*, 5937–5950. [CrossRef]
38. Pradhan, S.; Toll, D.G.; Rosser, N.J.; Brain, M.J. An investigation of the combined effect of rainfall and road cut on landsliding. *Eng. Geol.* **2022**, *307*, 106787. [CrossRef]
39. Tan, D.; Xu, X.; Wang, L.; Xu, J.; Shi, Q. Deformation evolution and failure mechanism of rainfall-induced granite residual soil landsliding event in Northern Guangdong, China: Tan et al. *Landslides* **2025**, *22*, 925–941. [CrossRef]
40. Bai, H.-L.; Feng, W.-K.; Li, S.-Q.; Ye, L.-Z.; Wu, Z.-T.; Hu, R.; Dai, H.-C.; Hu, Y.-P.; Yi, X.-Y.; Deng, P.-C. Flow-slide characteristics and failure mechanism of shallow landslides in granite residual soil under heavy rainfall. *J. Mt. Sci.* **2022**, *19*, 1541–1557. [CrossRef]
41. Raia, S.; Alvioli, M.; Rossi, M.; Baum, R.L.; Godt, J.W.; Guzzetti, F. Improving predictive power of physically based rainfall-induced shallow landslide models: A probabilistic approach. *Geosci. Model Dev.* **2014**, *7*, 495–514. [CrossRef]
42. Gu, T.; Duan, P.; Wang, M.; Li, J.; Zhang, Y. Effects of non-landslide sampling strategies on machine learning models in landslide susceptibility mapping. *Sci. Rep.* **2024**, *14*, 7201. [CrossRef]
43. Zhu, A.-X.; Miao, Y.; Liu, J.; Bai, S.; Zeng, C.; Ma, T.; Hong, H. A similarity-based approach to sampling absence data for landslide susceptibility mapping using data-driven methods. *CATENA* **2019**, *183*, 104188. [CrossRef]
44. Chang, Z.; Huang, J.; Huang, F.; Bhuyan, K.; Meena, S.R.; Catani, F. Uncertainty analysis of non-landslide sample selection in landslide susceptibility prediction using slope unit-based machine learning models. *Gondwana Res.* **2023**, *117*, 307–320. [CrossRef]
45. Liu, L.-L.; Zhao, S.-L.; Yang, C.; Zhang, W. Quantifying uncertainty in landslide susceptibility mapping due to sampling randomness. *Int. J. Disaster Risk Reduct.* **2024**, *114*, 104966. [CrossRef]
46. Merghadi, A.; Yunus, A.P.; Dou, J.; Whiteley, J.; ThaiPham, B.; Bui, D.T.; Avtar, R.; Abderrahmane, B. Machine learning methods for landslide susceptibility studies: A comparative overview of algorithm performance. *Earth Sci. Rev.* **2020**, *207*, 103225. [CrossRef]
47. Akinci, H.; Ozalp, A.Y. Investigating the effects of different data classification methods on landslide susceptibility mapping. *Adv. Space Res.* **2025**, *75*, 3427–3450. [CrossRef]
48. Huang, F.; Yang, Y.; Jiang, B.; Chang, Z.; Zhou, C.; Jiang, S.-H.; Huang, J.; Catani, F.; Yu, C. Effects of different division methods of landslide susceptibility levels on regional landslide susceptibility mapping. *Bull. Eng. Geol. Environ.* **2025**, *84*, 276. [CrossRef]
49. Marra, F.; Destro, E.; Nikolopoulos, E.I.; Zoccatelli, D.; Creutin, J.D.; Guzzetti, F.; Borga, M. Impact of rainfall spatial aggregation on the identification of debris flow occurrence thresholds. *Hydrol. Earth Syst. Sci.* **2017**, *21*, 4525–4532. [CrossRef]
50. Brunetti, M.T.; Melillo, M.; Gariano, S.L.; Ciabatta, L.; Brocca, L.; Amarnath, G.; Peruccacci, S. Satellite rainfall products outperform ground observations for landslide prediction in India. *Hydrol. Earth Syst. Sci.* **2021**, *25*, 3267–3279. [CrossRef]
51. Fell, R.; Corominas, J.; Bonnard, C.; Cascini, L.; Leroi, E.; Savage, W.Z.; on behalf of the JTC-1 Joint Technical Committee on Landslides and Engineered Slopes. Guidelines for landslide susceptibility, hazard and risk zoning for land use planning. *Eng. Geol.* **2008**, *102*, 85–98.

Disclaimer/Publisher's Note: The statements, opinions and data contained in all publications are solely those of the individual author(s) and contributor(s) and not of MDPI and/or the editor(s). MDPI and/or the editor(s) disclaim responsibility for any injury to people or property resulting from any ideas, methods, instructions or products referred to in the content.